Geologos 19, 4 (2013): 301–320
DOI: 10.2478/logos-2013-0019

GEOLOGOS

First report on the occurrence of CO_2-bearing fluid inclusions in the Meiduk porphyry copper deposit, Iran: implications for mineralisation processes in a continental collision setting

Sina Asadi[1*], Farid Moore[1], Alireza Zarasvandi[2] & Majid Khosrojerdi[3]

[1] Department of Earth Sciences, Faculty of Sciences, Shiraz University, Shiraz, Iran;
email: geosinaa@gmail.com; moore@susc.ac.ir
[2] Department of Geology, Faculty of Sciences, Shahid Chamran University, Ahvaz, Iran; email: zarasvandi_a@scu.ac.ir
[3] National Iranian Copper Industries Company (NICICo.), Sarcheshmeh, Iran; email: m_khosrojerdi@nicico.com
* corresponding author

Abstract

Hydrothermal alteration of the Meiduk porphyry copper deposit, south of the Kerman Cenozoic magmatic arc and southeast of the central Iranian volcano-plutonic belt has resulted in three stages of mineralisation characterised by veins and veinlets. These are, from early to late: (1) quartz + K-feldspar + biotite + pyrite ± chalcopyrite ± pyrrhotite ± magnetite (early potassic alteration and type-A veins); (2) quartz + chalcopyrite + pyrite + bornite + pyrrhotite + K-feldspar + biotite + magnetite (potassic-sericitic alteration and type-B veins); and (3) quartz + pyrite + chalcopyrite + sericite (sericitic alteration and type-C veins). Most ores were formed during stages 2 and 3.

Three main types of fluid inclusions are distinguished based on petrographical, microthermometrical and laser Raman spectroscopy analyses, i.e. type I (three-phase aqueous inclusions), type II (three-phase liquid-carbonic inclusions) and type III (multi-phase solid inclusions). The fluid inclusions in quartz veins of the stages are mainly homogenised at 340–530°C (stage 1), 270–385°C (stage 2) and 214–350°C (stage 3), respectively, with salinities of 3.1–16 wt.% NaCl equivalent, 2.2–43 wt.% NaCl equivalent and 8.2–22.8 wt.% NaCl equivalent, respectively.

The estimated trapping pressures are 97.9–123.6 MPa (3.7–4.6 km) in stage 1 and 62.5–86.1 MPa (2.3–3.1 km) in stage 2, respectively. These fluid inclusions are homogenised in different ways at similar temperatures, suggesting that fluid boiling took place in stages 2 and 3. The fluid system evolved from high-temperature, medium-salinity, high-pressure and CO_2-rich to low-temperature, low-pressure, high-salinity and CO_2-poor, with fluid boiling being the dominating mechanism, followed by input of meteoric water. CO_2 escape may have been a factor in increasing activities of NaCl and S^{2-} in the fluids, diminishing the oxidation of the fluids from stage 1 to 3. The result was precipitation of sulphides and trapping of multi-phase solid inclusions in hydrothermal quartz veins.

Keywords: CO_2-bearing fluid inclusions, laser Raman spectroscopy, collision, Meiduk porphyry copper deposit, Iran

1. Introduction

Porphyry copper deposits (PCDs) form commonly in association with the emplacement and crystallisation of silicic epizonal intrusions derived from hydrous arc magmas generated during partial melting of subducted oceanic crust (e.g., Wang *et al.*, 2006) and/or from a thickened juvenile mafic lower crust (e.g., Hou *et al.*, 2004; Hou & Cook 2009; Karsli *et al.*, 2010; Topuz *et al.*, 2011). According to early metallogenic models, porphyry systems

form in subduction-related magmatic arcs such as the Circum-Pacific porphyry copper belt, with no granitoid magmatism and mineralisation (Guild, 1972). Based on studies of mineralisations in the collisional Alpine-Himalayan orogenic belt, several (e.g., Chen & Fu, 1992; Chen *et al.*, 2007; Shafiei *et al.*, 2009; Haschke *et al.*, 2010) indicate, however, that a collisional orogenic setting is favourable for the development of adakitic magmatism and porphyry copper mineralisation. Several tectonic models for collisional orogenesis have been proposed by various authors; they have been summarised by Pirajno (2009).

Copper mineralisation in PCDs is mainly controlled by the behaviour of reduced sulphur, S^{2-} (Liang *et al.*, 2009), which inevitably requires the reduction of sulphate (S^{6+}: HSO^{4-}/SO_4^{2-}) in the initial oxidised source magma to sulphides (S^{2-}: $H_2S/HS^-/S^{2-}$) or polysulphides (e.g., S_2^{2-}, S^{3-}) during deposition (Sun *et al.*, 2013). The final phase of mineralisation in PCDs is attributed to magnetite crystallisation (i.e. ferrous iron oxidation), which induces sulphate reduction and accompanying oxygen-fugacity fluctuations during potassic alteration (Sun *et al.*, 2004; Liang *et al.*, 2009).

The Urumieh-Dokhtar magmatic belt in Iran was interpreted by Dewey *et al.* (1973) as an Andean-type Cordilleran arc system within the collisional Alpine-Himalayan orogenic belt, reflecting subduction and collision of the Afro-Arabian plate with Eurasia. All known porphyry copper deposits of Iran occur within the so-called Cenozoic Urumieh-Dokhtar magmatic belt. Cenozoic tectono-magmatic activity and porphyry copper mineralisation along the Urumieh–Dokhtar magmatic system is attributed by various authors to three time-windows: (1) Eocene-Oligocene (Ahmadian *et al.*, 2009); (2) mid-late Oligocene (Kirkham & Dunne, 2000; McInnes *et al.*, 2005); and (3) mid-late Miocene (McInnes *et al.*, 2005; Razique *et al.*, 2007; Richards *et al.*, 2012). The majority of the authors, however, believe that the main porphyry Cu mineralisation occurred during the Miocene (e.g., Zarasvandi *et al.*, 2005, 2007, Taghipour *et al.*, 2008; Shafiei *et al.*, 2009; Haschke *et al.*, 2010).

The Meiduk porphyry copper system is located at the southern edge of the Kerman Cenozoic magmatic arc (KCMA; Shafiei *et al.*, 2009) in the Shahr-Babak area. Meiduk and a number of subeconomic porphyry copper deposits (e.g., Iju and Chah Firuzeh) are all associated with middle to late Miocene diorite/granodiorite to quartz-diorite stocks in the region. So far, more than sixty diamond drill holes (>8000 m) with a maximum depth of 1100 m have proved the presence of a sizeable and potentially economic porphyry copper mineralisation of the Meiduk deposit. Evaluation of the deposit by National Iranian Copper Industries Company (NICICo.) outlines the ore reserve as around 170 million tonnes, with on average 0.86% Cu, 0.007% Mo, 82 ppb Au and 1.8 ppm Ag (Taghipour *et al.*, 2008); the total resources are, however, known to be considerably larger than 170 million tonnes, because high-grade hypogene mineralisation continues at depths of over 1 km (Boomeri *et al.*, 2009).

Moore (1992) was the first to present details of the geology, alteration and fluid inclusions of the deposit. On the basis of mineralogy, fluid-inclusion studies and hydrothermal-alteration assemblages, Taghipour *et al.* (2008) and Hezarkhani (2008) suggested that late boiling occurred in the upper part of the sericitic zone associated with significant chalcopyrite precipitation during inflow of oxidised, acidic meteoric water and cooling of the system. Boomeri *et al.* (2009) came to a similar conclusion.

CO_2-rich fluid inclusions have been commonly reported from different types of metallic ore deposits (e.g., skarns and orogenic lode systems) and petroleum and basinal fluids (e.g., Dubessy *et al.*, 2001; Hurai *et al.*, 2002; Robb, 2005; Shen *et al.*, 2010; Asadi *et al.*, 2013). These inclusions are, however, typically not present in most porphyry Cu deposits, but CO_2 has been identified in inclusions from some porphyry Cu deposits (e.g. from Butte: Rusk & Reed 2002; from Bajo de la Alumbrera: Ulrich *et al.*, 2002; from Bingham: Redmond *et al.*, 2004; Landtwing *et al.*, 2005; and from El Teniente: Klemm *et al.*, 2007; Rusk *et al.*, 2008; Landtwing *et al.*, 2010). By contrast, fluid inclusions in several quartz veins from the Meiduk porphyry Cu deposit are CO_2-rich. The presence of CO_2 in fluid inclusions in the Meiduk porphyry is reported here for the first time.

To elucidate the evolutionary history of CO_2-rich fluids and the origin of the Meiduk Cu deposit further, the present contribution focuses on the origin and composition of the fluid during the mineralisation that was associated with potassic and sericitic alterations. In order to achieve this goal, the field relationships, vein mineralogy, and microthermometry of the fluid inclusions were investigated, the oxygen fugacity (fO_2) was calculated, and laser Raman spectroscopy analysis was applied.

2. Regional geology

The magmatic and tectonic evolution of the KCMA in the south-eastern part of the Urumieh-Dokhtar arc system was influenced by the subduction of the Tethyan oceanic lithosphere under the central Iran microcontinent during the Eocene (e.g., Shahabpour, 2005; Alavi, 2007; Shafiei, 2010). Richards *et al.* (2012) believe that such a setting probably represents a developed magmatic arc on the central Iran microcontinent on top of a Neotethyan subduction zone that dipped toward the north-east. Dercourt *et al.* (1986) proposed that the KCMA resulted from steep and oblique subduction of Neotethyan oceanic lithosphere under a rotating central Iran microcontinent and parts of a small ocean during the Eocene. The pre-collisional Eocene volcanic and intrusive suites show a calc-alkaline and locally tholeiitic affinity with a subduction-related island-arc setting (Shahabpour, 2005).

The end of the NE-directed oblique subduction and collision during the Palaeogene was connected with intra-arc and back-arc extension, magmatism and dextral strike-slip faults and thrusts in the KCMA (McClusky *et al.*, 2000; McClay *et al.*, 2004). Mohajjel *et al.* (2003) proposed a Miocene age for the continental collision between the Afro-Arabian margin and Eurasia, based on the imbricate system and development of blind thrusting and folding in the Zagros Fold-Thrust Belt. Based on the $^{40}Ar/^{39}Ar$ and Rb/Sr ages of 11.3±0.5 Ma and 12.4±0.2 Ma, respectively (Hassanzadeh, 1993), for the Meiduk intrusives, it may be concluded that the collision between the Afro-Arabian margin and central Iranian plates occurred during the late Neogene. Shafiei (2008) and Shafiei *et al.* (2009) suggested, based on previous gravimetric studies by Dehghani

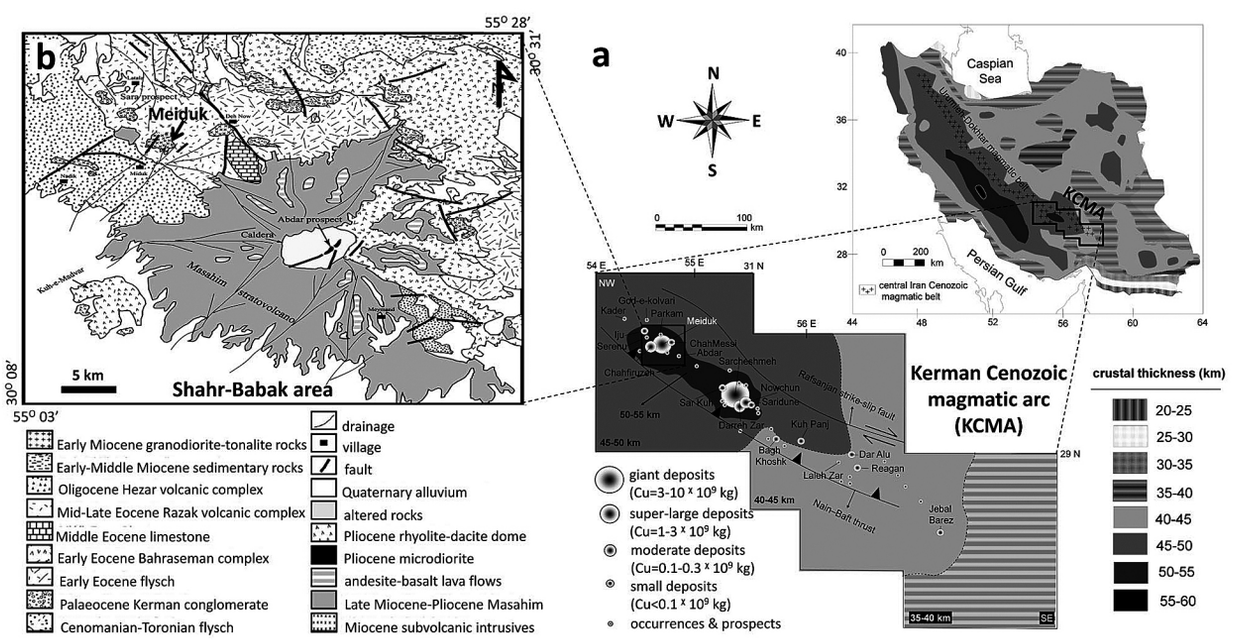

Fig. 1. Geological setting. **a:** Moho depths (grey shaded) and crustal thickness (km) in the KCMA with distribution and size of porphyry Cu deposits and prospects (after Saric & Mijalkovic, 1973). Inset: contour map of present-day crustal thicknesses in Iran (simplified after Dehghani & Makris, 1983; modified after Shafiei *et al.*, 2009); **b:** Geological map of the Shahr-Babak area and location of the Meiduk porphyry (modified after Dimitrijevic, 1973).

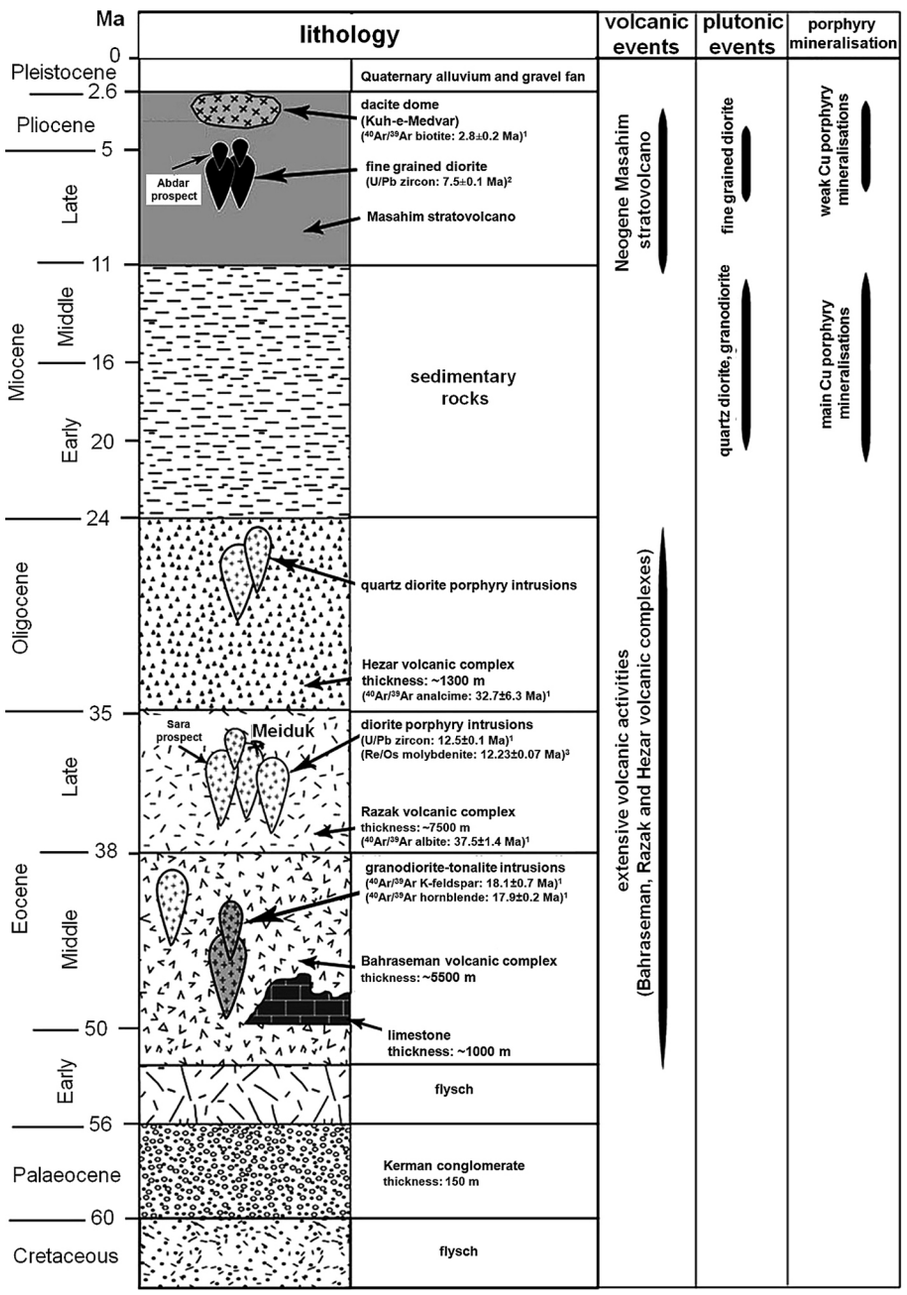

Fig. 2. Stratigraphic succession, volcano-plutonic events and porphyry copper mineralisation episodes in the Shahr-Babak area and location of Meiduk porphyry (dating from (1) Hassanzadeh 1993; (2) McInnes *et al.* 2005 and (3) Taghipour *et al.* (2008).

& Makris (1983), that collision-related shortening produced a thickened crust of the order of 45–55 km (Fig. 1a), especially in the central and north-western parts (e.g., the Meiduk region) of the KCMA. This mid-Miocene orogenic magmatism formed adakite-like porphyritic granodiorites without volcanic equivalents, which host several world-class copper deposits (e.g. Meiduk: Hou *et al.*, 2011).

The Meiduk area is located on the La Chah Mountain, about 3 km north-east of the village of Meiduk and 46 km from Shahr-Babak City (Fig. 1b). The Meiduk porphyry lies in a basin confined within a curved ridge (Hezarkhani 2008). In the study area, the regional structures comprise a series of major NW-SE trending Palaeogene volcano-sedimentary rocks.

Stratigraphically, the Meiduk area is composed of three volcanic successions (Hassanzadeh, 1993) (Fig. 2): (1) the early Eocene Bahraseman complex, comprising acidic pyroclastics, tuffs, volcanic breccias, mostly trachybasaltic to trachyandesitic, (2) the mid-late Eocene Razak complex ($^{40}Ar/^{39}Ar$ age of albite 37.5±1.4

Ma), composed mainly of basaltic-rhyolitic volcaniclastic rocks, and (3) the Oligocene Hezar complex ($^{40}Ar/^{39}Ar$ age of analcime: 32.7±6.3 Ma) of trachyandesites and trachybasalts. The Razak volcanic complex (~7500 m thickness) is the main host rock of the Meiduk porphyry.

According to McInnes *et al.* (2005) the U/Pb and U-Th/He zircon age of the Meiduk deposit is 12.5 Ma (Table 1). The mineral whole-rock Rb-Sr age of the Meiduk porphyry is reported as 12.4±0.2 Ma, but it must be mentioned here that the Rb-Sr age data do not seem to be reliable due to Rb addition and Sr depletion during potassic alteration (Hassanzadeh, 1993). Hassanzadeh (1993) reported the ages of the potassic and sericitic alteration events using $^{40}Ar/^{39}Ar$ dating; the age of the potassic alteration zone, based on biotite and K-feldspar, is 11.3±0.5 Ma and 11.2±0.4 Ma, respectively, whereas the $^{40}Ar/^{39}Ar$ isochron age for sericite in the sericitic alteration zone was also found to be 10.8±0.4 Ma (Hassanzadeh, 1993; Table 1). The Re-Os molybdenite data provide the timing of sulphide mineralisation at 12.23±0.07 Ma for the Meiduk porphyry (Taghipour *et al.*, 2008; Table 1).

Petrographical observations of thin sections indicate that the Meiduk porphyry is strongly altered and contains 40–50 vol% of phenocrysts consisting mainly of plagioclase, quartz, biotite and hornblende. The original composition of the plagioclases is unclear because all of them have been altered, as well as the hornblende and the biotite. The matrix of this intrusive phase consists mainly of fine-grained quartz, biotite, titanite, apatite, plagioclase, K-feldspar and anhydrite.

3. Hydrothermal alteration and relationships between copper and the quartz veins

Several types of hydrothermal alteration at the Meiduk porphyry deposit have been studied (IGME-INOMRM, 1973; Hassanzadeh, 1993; Taghipour *et al.*, 2008). These alteration types extend upward sand outwards several kilometres from the deposit's centre and they show zoning in space and time. Three distinct types of hydrothermal alteration and mineralisation have been recognised at Meiduk: (a) a hypogene zone, (b) a supergene sulphides zone; and (c) an oxidised or leached zone.

The alterations at Meiduk include: (1) potassic alteration, with biotite and feldspar as predominant hydrothermal minerals; (2) a transitional potassic-sericitic zone, characterised mainly by K-feldspar, biotite and sericite, with minor albite, tourmaline and chlorite; (3) sericitisation, characterised by the transformation of feldspar and biotite into sericite, with disseminated pyrite and quartz-sericite veins and veinlets; (4) argillisation, characterised by transformation of feldspar into smectite or kaolinite, usually controlled by fractures; (5) propylitisation, with epidote, chlorite and calcite as predominant hydrothermal minerals (Taghipour *et al.*, 2008).

Based on cross-cutting relationships among minerals and mineral assemblages, the mineralisation in the Meiduk system can be divided into three episodes of vein formation (Fig. 3 a-h).

Table 1. Radiometric age of Meiduk porphyry and associated hydrothermal alterations.

sample material	dating method	age (Ma)	source
sericite (sericitic zone)	$^{40}Ar/^{39}Ar$	10.8±0.4	Hassanzadeh (1993)
K-feldspar (potassic zone)	$^{40}Ar/^{39}Ar$	11.2±0.4	Hassanzadeh (1993)
biotite (potassic zone)	$^{40}Ar/^{39}Ar$	11.3±0.5	Hassanzadeh (1993)
whole rock	Rb-Sr	12.4±0.2	Hassanzadeh (1993)
single zircon	U-Pb	12.5 ±0.1	McInnes *et al.* (2005)
single zircon	U-Th/He	12.5 ± 0.5	McInnes *et al.* (2005)
molybdenite	Re-Os	12.23±0.07	Taghipour *et al.* (2008)

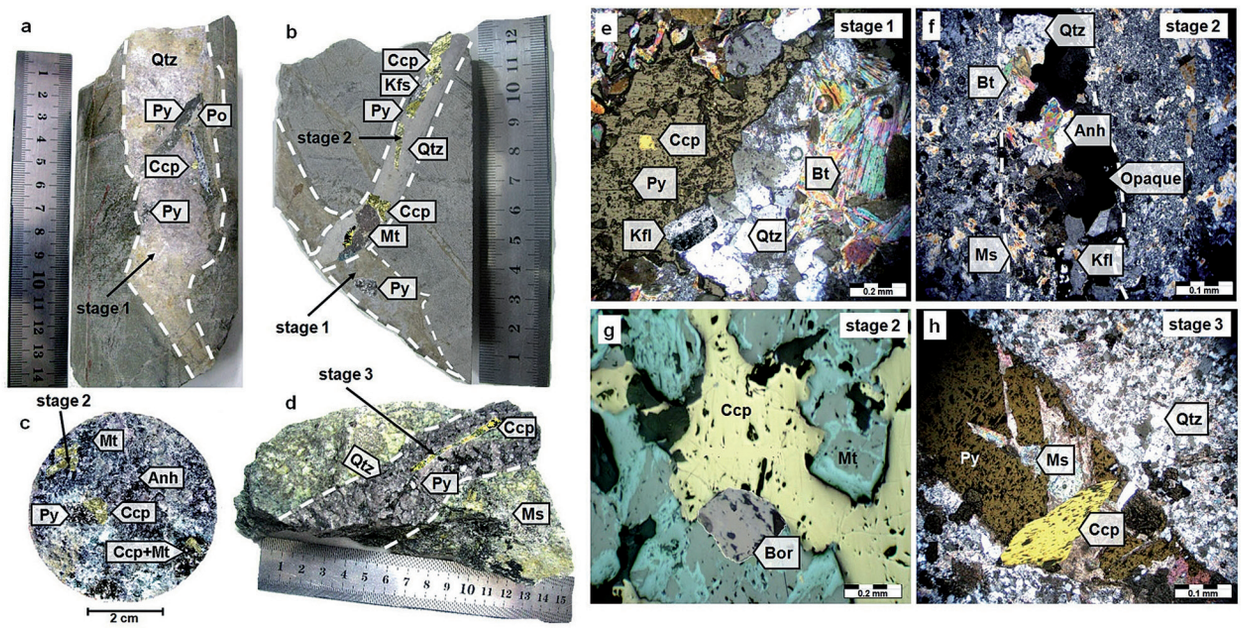

Fig. 3. Macro (a-d) and microphotographs (e-h) of the ore and gangue vein minerals from the Meiduk deposit. **a:** stage 1: early quartz vein (type-A vein; early potassic alteration) (Qtz = quartz, Ccp = chalcopyrite, Py = pyrite, Po= pyrrhotite); **b–c:** Stage 2: main quartz vein (type-B vein; potassic-sericitic alteration) cuts type-A vein (stage 1) (Kfs = K-feldspar, Anh = anhydrite, Mt = magnetite); **d:** Stage 3: late quartz vein (type-C vein; sericitic alteration) (Ms = muscovite); **e:** Polished thin section of silicate and ore-mineral assemblages in a type-A vein (stage 1) consisting of quartz + K-feldspar + biotite (Bt) + chalcopyrite; crossed nicols; **f:** Polished thin section of silicate and ore-mineral assemblages in a type-B vein(stage 2) consisting of quartz + K-feldspar + biotite + anhydrite + opaque minerals; crossed nicols; **g:** Polished section of chalcopyrite + bornite (Bor) + magnetite in stage 2; reflected light; **h:** Polished thin section of silicate and ore-mineral assemblages in a type-C vein (stage 3) consisting of quartz + sericite + chalcopyrite + pyrite; crossed nicols.

3.1. Stage 1: early quartz veins (type-A veins)

The earliest quartz type is characterised by the assemblage of K-feldspar, quartz, biotite, pyrite and minor amounts of pyrrhotite and magnetite. Pyrite is mostly disseminated and coexists with K-feldspar and epidote; pyrite occurs as hypidiomorphic cubes; minor chalcopyrite amounts are scattered in the porphyry.

Type-A veins occur in the pre-ore stage (stage 1) located in the centre and the deepest parts of the Meiduk system, and associated with early potassic alteration (Fig. 3 a, e). Structural irregularities suggest that the veins formed at relatively high temperatures, when the rock was relatively ductile, probably shortly after the stock consolidated; they vary in width from 1 to >5 cm.

3.2. Stage 2: Main quartz veins (type-B veins)

The potassic-sericitic alteration is directly associated with abundant stockwork quartz-rich veins and includes euhedral quartz-chalcopyrite-pyrite-bornite-pyrrhotite-K-feldspar-biotite and anhedral anhydrite (Fig. 3 b, c, f, g). Magnetite displays a dissemination form within quartz-sulphide veins. Secondary K-feldspar, sericite and clay minerals are commonly present adjacent to the vein where plagioclase phenocrysts are intersected and biotite is altered to secondary biotite, sericite and rutile aggregates. They occur throughout the potassic-sericitic alteration zone and extend into the adjacent volcanic wall rocks of the Razak complex. They are interpreted to have been emplaced during waning stages of the potassic alteration.

Type-B veins are typically irregular in width (generally >10cm). These veins generally cut type-A veins (Fig. 3b).

3.3. Stage 3: late quartz veins (type-C veins)

Sericitic alteration forms selvages typically a few centimetres wide (3–10cm) along structurally controlled type-C veins that lie on fractures and faults. Where these veins are closely spaced, the alteration is pervasive in volumes up to 1 km^3. Sulphides are commonly strongly zoned from central chalcopyrite-rich veins cutting the potassic-sericitic ore zone upwards and outwards to pyrite-chalcopyrite veins to pyrite-dominated veins (Fig. 3 d,h). Type-C veins tend to be pyrite-rich with obvious sericitic alteration halos (including quartz and sericite) formed within the Meiduk porphyry as well as in the adjacent wall rocks.

3.4. Relationship between copper mineralisation and the vein types

Copper mineralisation at the Meiduk system appears to be dominated volumetrically by type-A, type-B and type-C veins, which are particularly abundant in the intermediate and deep parts of the intrusion, corresponding to the potassic, potassic-sericitic and sericitic alteration zones, respectively.

4. Methods applied to the research of the fluid inclusions

Microthermometric measurements were made using a Linkam THMSG600 with a combined heating and freezing stage with a temperature range of –196 to +600 °C, attached to an Olympus petrographical microscope with LinkSys software (version 1.83). The reproducibility of the measurements was better than ±0.2°C for temperatures of less than 30°C and ±2°C at a total homogenisation temperature when the chips were centred in the specimen holder. Stage calibration was carried out at –56.6°C (pure CO_2), 0.0°C (H_2O), and 340°C (H_2O) using standard synthetic fluid inclusions. Ice-melting temperatures were determined at a heating rate of no more than 0.1°C/s. Homogenisation temperatures were determined at a heating rate of 1°C/s. Homogenisation of multi-phase solid inclusions was obtained with heating cycles of about 5°C. For two-phase inclusions, the homogenisation temperature of liquid and vapour (predominant LV→L and rare LV→V) was recorded. In the multi-phase solid inclusions, two points were recorded: (1) $T_{h(NaCl)}$ (the temperature at which halite dissolves) and (2) $T_{h(LV)}$ (the temperature of vapour and liquid homogenisation).

Fifty core samples from the hypogene alteration zones (potassic, potassic-sericitic and sericitic) and several vein types from various depths were collected for laboratory analyses. Over forty samples were investigated for the types of inclusion, their abundance, spatial distribution, and size. Thirty quartz wafers were polished at both sides using the procedure of Shepherd *et al.*, (1985). The thickness of the wafers varied between 100 and 150 μm, depending on the transparency of the quartz crystals. Sample selection was biased to quartz containing an abundance of ore-related sulphide minerals in type-A, type-B and type-C veins.

The bulk compositions, pressure range, density and mole fractions of CO_2, H_2O and NaCl (XCO_2, XH_2O and XNaCl) were calculated using equations of state (Bowers & Helgeson, 1983, for H_2O-CO_2-NaCl fluid inclusions; Zhang & Frantz, 1987, for H_2O-NaCl fluid inclusions) in computer programs MacFlinCor (Brown & Hagemann, 1994) and FLUIDS (Bakker, 2003).

The salinities of H_2O-CO_2-NaCl and NaCl-H_2O inclusions were calculated using the final melting temperatures of CO_2-clathrate (Collins, 1979) and ice points (Bodnar, 1993), respectively. The salinities of multiphase-bearing fluid inclusions were calculated using the dissolution temperatures of daughter minerals (Hall *et al.*, 1988). Because the opaque daughter minerals do not melt during the heating process, the salinities presented here do not include the contribution of these opaque daughter minerals.

The densities of H_2O-CO_2-NaCl and NaCl-H_2O inclusions were calculated using the Flincor procedure (Brown, 1989). In addition, laser Raman spectroscopy was applied to vapour phases in selected inclusions at Geoscience Lab Australia, using a Dilor SuperLabram laser Raman microprobe with a spatial resolution of <1 μm, following the method of Burke (2001). The laser beam with a wavelength of 514.5 nm and a spot size of about 1 μm was focused on the bubble for each fluid inclusion through a light microscope.

5. Petrography of the fluid inclusions

The petrographical characteristics of the fluid inclusions were, as well as their morphology, recorded at room temperature following Roedder (1984) and Shepherd *et al.* (1985). The criterion used for the recognition of primary inclusions was that the inclusions were distributed individually or in random clusters (Roedder, 1984). Based on petrographical and microthermometrical studies and phases present at temperature room, the inclusions were divided into the following types (Fig. 4 a-f). Type-I consists of three-phase aqueous inclusions (liquid+vapour±solid), type-II of three-phase liquid-carbonic inclusions (LH_2O+LCO_2+V), type-III of multi-phase solid inclusions, type-IV of monophase liquid inclusions (aqueous liquid), and type-V of monophase gaseous inclusions.

Type-I inclusions consist of liquid+vapour±solid phases with the liquid phase being volumetrically dominant. These fluid inclusions are common in all mineralised quartz veins. The sizes of these fluid inclusions range from 11 to 18 μm. These inclusions have a de-

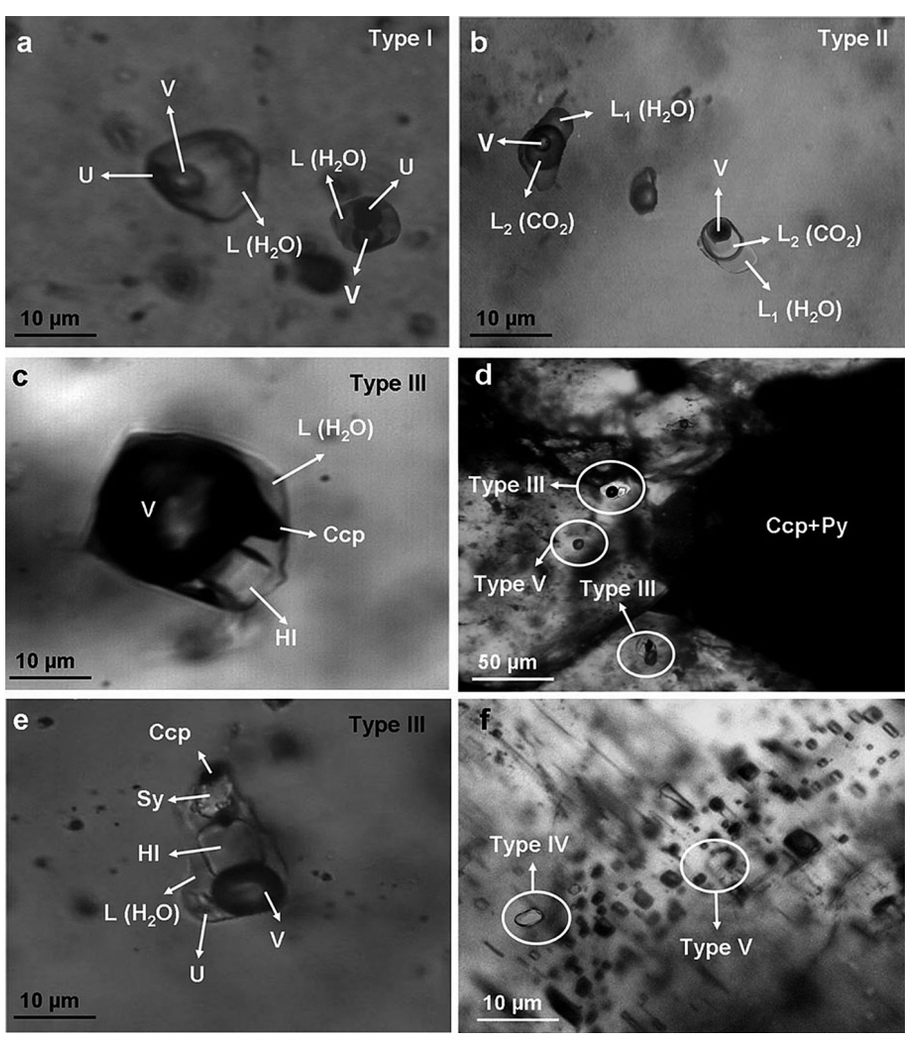

Fig. 4. Photomicrographs showing fluid-inclusion types in quartz veins of the Meiduk mine. Abbreviations: L(H_2O) = H_2O liquid; L(CO_2) = CO_2 liquid; V = vapour; Hl = halite; Sy = sylvite; U = unknown solid or daughter phases; Ccp = chalcopyrite; Py = pyrite. **a:** Type-I fluid inclusions, two-phase aqueous inclusions (liquid + vapour ± solid); **b:** Type-II fluid inclusions, three-phase liquid-carbonic inclusions (LH_2O + LCO_2 + V); **c:** Type-III fluid inclusions, multi-phase solid inclusions; **d:** Possible co-occurrence of type-III (multi-phase solid inclusions) and type-V (gaseous type) fluid inclusions in a type-B vein (boiling process) and close relationship between both types (III and V inclusions) and sulphide minerals (e.g., Ccp = chalcopyrite and Py = pyrite) in a type-B vein (stage 2); **e:** Type-III fluid inclusions; **f:** Type-IV (monophase liquid) and type-V (monophase gaseous) fluid inclusions in Meiduk quartz veins.

gree of fill (F) typically of 0.7 and rarely ~0.5. In a small number of type-I inclusions, unidentified transparent or opaque minerals are present. The distribution and volume of solid phases are irregular (2–10%), suggesting that they represent trapped solids rather than daughter minerals. They are isolated or most commonly form trails and clusters in the veins. The relative abundances of type-I inclusions increase from stage 1 to stage 3.

Type-II inclusions are three-phase liquid-rich (F = ~0.6) inclusions, up to 10 μm in size and are negative crystal in shape (hexagonal). They occur as isolated clusters, suggesting a primary origin. Liquid CO_2 is evident at room temperature as a dark boundary in the inner wall. The populations of type-II inclusions decrease from stage 1 to stage 2 and from deep to shallow levels.

Type-III inclusions are, at room temperature, multi-phase solid inclusions. Generally, they have negative crystal shapes, and are typically 10–20 μm in size. These inclusions contain at room temperature liquid plus daughter phases plus 10–20 vol.% vapour. The daughter phase is predominantly halite (cubic shape), occasionally accompanied by sylvite (rounded shape); therefore, almost all inclusions measured are halite-bearing inclusions and $T_{h(KCl)}$ (the temperature at which sylvite dissolves) was not recorded.

The solid phases (mostly sulphides such as chalcopyrite) and unidentified opaque minerals seldom constitute more than 1% by volume of an inclusion and therefore do not significantly affect its homogenisation temperature. Type-III inclusions are commonly scattered variably in all mineralised quartz veins, but in stages 1 and 3 mostly contain transparent daughter minerals (e.g., halite and/or sylvite) that homogenised to the liquid or vapour before total homogenisation by halite dissolution. This is what Wilkinson (2001) termed "halite undersaturated inclusions" for porphyry copper deposits. The populations of type-III inclusions increase from stage 1 to stage 3 and in particular in stage 2.

Type-IV inclusions contain at room temperature one-phase liquid. These inclusions may be irregular and/or rectangular in shape. The diameters of these fluid inclusions range from 3 to 5 μm. These fluid inclusions are common in all mineralised quartz veins.

Type-V inclusions are divided, according to their filling ratio, into V_1 inclusions (~65% vapour) and V_2 inclusions (>90% vapour). Both types commonly have a rounded isometric shape and are 4–7 μm in size. They are scattered in individual quartz veins. These inclusions are generally dark and show no visible aqueous phase at room temperature. Type-V inclusions are mostly scattered variably in type-B veins.

Type-IV and type-V fluid inclusions in the Meiduk quartz veins are small (<7 μm) and monophase (liquid or gaseous); hence they were not chosen for microthermometrical studies. Types I, II and III constitute the majority of fluid inclusions in the quartz veins (Table 2; type-A veins and stages 1: IA, IIA and IIIA; type-B veins and stages 2: IB, IIB and IIIB; type-C veins and stages 3: IC and IIIC) and account for 85% of the inclusion population. They were chosen for microthermometrical studies for two important reasons: (1) the inclusions are intimately associated with copper sulphides, and (2) these types contain inclusions >10 μm, which allows for more confident thermometrical analysis. In addition, primary fluid inclusions, as far as without evidence of necking down, were selected for microthermometrical analyses (cf. Roedder, 1984). All variations indicate that the ore-forming fluids changed from carbonic to aqueous along with time and with upward migration from stage 1 to stage 3.

6. Results of microthermometrical and Laser Raman Spectroscopy

The microthermometrical data of fluid inclusions are summarised in Table 2 and Figure 5 (a-f), which clearly show the relationships between mineral assemblages, physical-chemical conditions and metallogenic stages.

The stage–1 quartz veins contain lots of IA, IIA, and minor IIIA fluid inclusions. The final ice-melting temperatures ($T_{m\text{-}ice}$) of type-IA fluid inclusions range between –10.1°C

Table 2. Summary of microthermometric data for primary fluid inclusions in Meiduk quartz veins.

inclusion types	vein type (stage of mineralisation)	phase	number	size (μm)	$T_{m\text{-}NaCl}$ (°C)	$T_{m\text{-}CO_2}$ (°C)
IA	A (1)	L+V±S	20	11 to 18	–	–
IIA	A (1)	L_1+L_2+V	30	11 to 20	–	–62.8 to –58.4
IIIA	A (1)	L+V±Hl±Sy±S	9	10 to 15	–	–
IB	B (2)	L+V±S	31	10 to 15	–	–
IIB	B (2)	L_1+L_2+V	17	15 to 25	–	–59.5 to –57.1
IIIB	B (2)	L+V±Hl±Sy±S	30	12 to 18	182 to 356	–
IC	C (3)	L+V±S	50	10 to 19	–	–
IIIC	C (3)	L+V±Hl±Sy±S	22	10 to 20	–	–

inclusion types	$T_{m\text{-}ice}$ (°C)	$T_{m\text{-}CLATH}$ (°C)	$T_{h\text{-}CO_2}$ (°C)	salinity (wt.% NaCl equiv)	T_h (°C)	pressure (MPa)
IA	–10.1 to –4.7	–	–	7.4 to 14.1	340 to 518	–
IIA	–	+3.5 to +8.4	23.2 to 30.4	3.1 to 11.2	369 to 530	97.9 to 123.6
IIIA	–12.1 to –6.8	–		10.2 to 16	380 to 515	–
IB	–6.2 to –2.4	–	–	3.9 to 9.4	270 to 342	–
IIB	–	+5.2 to +8.9	–	2.2 to 8.6	281 to 380	62.5 to 86.1
IIIB	–	–	–	31 to 43	316 to 385	–
IC	–7.4 to –5.3	–	–	4.7 to 10.9	214 to 336	–
IIIC	–20.7 to –8.4	–	–	12.2 to 22.8	263 to 350	–

Notes: T_h: homogenisation temperatures; $T_{m\text{-}ice}$: final ice melting temperature; $T_{m\text{-}CO_2}$: melting temperature of CO_2 phase; $T_{m\text{-}CLATH}$: dissolution temperature of CO_2 clathrate; $T_{m\text{-}NaCl}$: dissolution temperature of halite; $T_{h\text{-}CO2}$: homogenisation temperature of CO_2 phase into the carbonic vapour phases. Abbreviation: L_1: H_2O-liquid; L_2: CO_2-liquid; V: vapour; S: solid phases (e.g., chalcopyrite); Hl: halite and Sy: sylvite.

and –4.7°C. These temperatures correspond to a moderate salinity of 7.4 to 14.1 wt.% NaCl equivalent. The homogenisation temperatures (T_h) of IA inclusions in early quartz veins vary between 340°C and 518°C (mean: 443°C), with densities of 0.62-0.78 g·cm^{-3}. The type-I-IA carbonic fluid inclusions melt between –62.8°C and –58.4°C ($T_{m\text{-}CO_2}$), which is lower than the

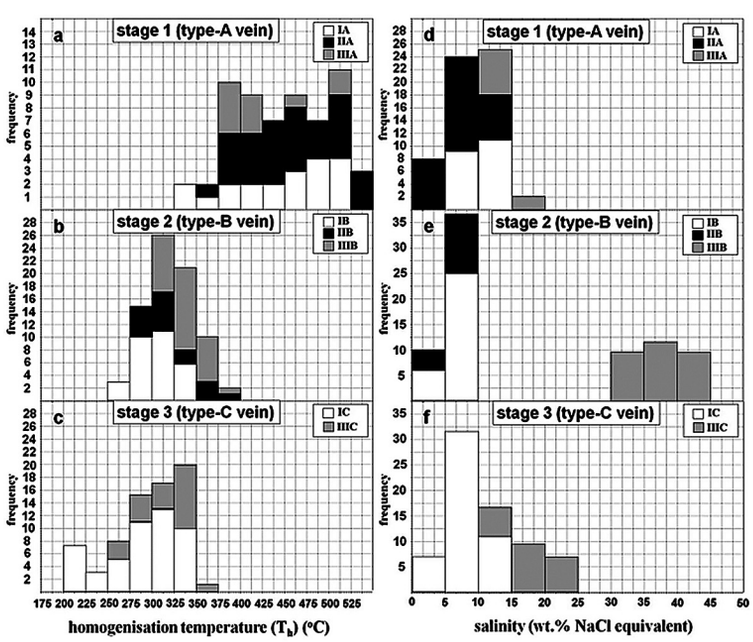

Fig. 5. Histograms of homogenisation temperatures (T_h) (°C) and salinities (wt.% NaCl equivalent) of fluid inclusions in different quartz veins.

melting temperature of pure CO_2 (triple-phase point is –56.6°C), suggesting minor amounts of dissolved CH_4 and/or N_2 in addition to CO_2 (Dreher *et al*., 2007; Volkov *et al*., 2011). Clathrate melting temperature values ($T_{m\text{-}CLATH}$) for this group is between +3.5°C and +8.4°C, corresponding to salinities of 11.2–3.7 wt.% NaCl equivalent, with a peak at around +7.1°C (5.5 wt.% NaCl equivalent). Estimated salinities are based on the assumption of pure H_2O-CO_2-NaCl. Type-IIA fluid inclusions are totally homogenised to liquid or vapour at temperatures ranging from 369°C to 530°C (T_h), concentrating between 380°C and 460°C. Some type-IIA fluid inclusions decrepitated before reaching homogenisation (usually above 380°C), probably because of increased internal pressure of CO_2 (cf. Roedder, 1984). The carbonic portion of most of the type-IIA fluid inclusions homogenised into a vapour phase, and their $T_{h\text{-}CO2}$ values span a range from +23.2°C to +30.4°C, which corresponds to a density range of 0.73-0.82 g·cm^{-3} for CO_2. In type-IIIA inclusions, $T_{m\text{-}ice}$ values fall between –12.1°C and –6.8°C, corresponding to a moderate salinity, between 16 and 10.2 wt.% NaCl equivalent. T_h values of type-IIIA fluid inclusions range from 380°C to 515°C (mean 432°C). The majority of the inclusions homogenised to a liquid phase (LV→L).

The fluid inclusions in stage 2 are IB, IIB, and IIIB types. In type-IB inclusions, $T_{m\text{-}ice}$ values vary from –6.2°C to –2.4°C, corresponding to salinities of 9.4 and 3.9 wt.% NaCl equivalent and densities of 0.62 to 0.94 g·cm^{-3}. They are mainly homogenised to liquid at temperatures between 270°C and 342°C. The type-IIB inclusions contain 20–40% CO_2 by volume at room temperature and yield a $T_{m\text{-}CO2}$ mainly ranging from –57.1°C to –59.5°C, suggesting a small quantity of other gases being dissolved in the carbonic phase. $T_{m\text{-}CLATH}$ occurs in the interval of +5.2°C to +8.9°C, corresponding to salinities of 8.6–2.2 wt.% NaCl equivalent and carbonic phase homogenised to vapour at temperatures from 18.6°C to 31.1°C ($T_{h\text{-}CO2}$). The total homogenisation temperatures ranging from 281°C to 380°C, peaking at 310°C, with densities of 0.77-0.84 g·cm^{-3}. In type-IIIB inclusions, chalcopyrite and unidentified solid minerals occur, which do not melt in heating runs, while the daughter halite dissolved at 182°C to 356°C ($T_{m\text{-}HCl}$), corresponding to high salinities of 31–43 wt.% NaCl equivalent. These hypersaline fluid inclusions are totally homogenised to liquid or vapour at temperatures of 316–385°C, with 345°C being the peak value, and densities of 0.76-0.98 g·cm^{-3}.

In stage 3, only IC and IIIC fluid inclusions are present in the quartz veins. The type-IC inclusions yield $T_{m\text{-}ice}$ values of –7.4°C to –2.3°C, corresponding to salinities of 10.9–4.7 wt.% NaCl equivalent. These fluid inclusions are totally homogenised to liquid at temperatures of 214°C to 336°C, and densities of 0.84-0.92 g·cm^{-3}. In type-IIIC inclusions, the $T_{m\text{-}ice}$ values fall between –20.7°C and –8.4°C, corresponding to a moderate salinity, between 12.2 and 22.8 wt.% NaCl equivalent. The homogenisation temperatures vary from 263°C to 350°C, with densities ranging from 0.88 to 0.90 g·cm^{-3}. The majority of the type-IIIC inclusions homogenised to a liquid phase (LV→L).

Laser Raman spectroscopy analysis on the vapour phase of five samples in type-IIA (2 samples) and type-IIB (3 samples) fluid inclusions generally reveals obvious peaks of CO_2 (1284 and 1390 cm^{-1}) and a small amount of CH_4 (2914 and 2916 cm^{-1}). This is in agreement with the microthermometrical results that the melting temperatures of solid CO_2 ($T_{m\text{-}CO_2}$) are lower than –56.6°C (Fig. 6).

7. Results and discussion

7.1. P-T conditions and oxygen fugacity (fO_2)

Considering the homogenisation temperatures, homogenisation behaviour and proportion of the CO_2 phase in the type-IIA and type-IIB inclusions, as well as the total homogenisation temperature of the inclusions, the trapping pressures were estimated using the Flincor program (Brown, 1989) and the formula of Bowers & Helgeson (1983) for the H_2O–CO_2–NaCl system.

The homogenisation temperatures of the type-IIA fluid inclusions (stage 1) used here are all above 320°C. The trapping pressure of

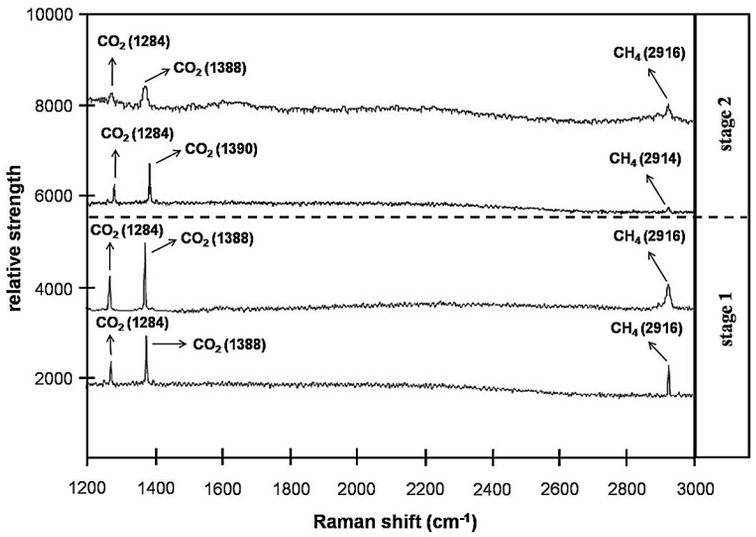

Fig. 6. Laser Raman spectra of fluid inclusions of the Meiduk deposit (stage 1: IIA inclusions; and stage 2: IIB).

the fluid inclusions was estimated to be 97.9 to 123.6 MPa, which corresponds to a depth of 3708 to 4681 m (assuming a constant pressure gradient of ~26.4 MPa per 1 km of depth). In contrast, inclusions in the type-IIB (stage 2), with a pressure below 86.1 MPa (62.5–86.1 MPa) and homogenisation temperatures between 281°C and 357°C correspond to depths of 2367–3147 m. No pressure estimation has been obtained for stage 3, due to the small amount of CO_2 phase in type IC and IIIC inclusions. This suggests that the trapping pressure of the fluid inclusions decreased from stage 1 to stage 2, which is similar to magmatic-hydrothermal systems in the Alpine-Himalayan orogenic belt (e.g., Yang *et al.*, 2009; Zhong *et al.*, 2011; Fan *et al.*, 2011; Li *et al.*, 2012; Asadi *et al.*, 2013).

Generally, the pressure decrease indicates that most of the magmatic-hydrothermal systems were formed in a rapid crust-uplift setting caused by synorogenic crustal thickening (such as KCMA) or post-orogenic delamination of the lithospheric root (Yang *et al.*, 2012). Hence it appears that the copper mineralisation in the Meiduk area took place mainly at depths of about 2300–3000 m, although the onset of the mineralisation probably took place at greater depths. The inferred depth interval coincides with the estimated mineralisation depth range (1–5 km) for other porphyry deposits in the world (e.g., Pirajno, 2009).

The oxygen fugacity (fO_2) and trapping conditions were also calculated for the full range of XCO_2, XH_2O and *X*NaCl at the assumed T-P range, using the equations and equilibrium constant of Ohmoto & Kerrick (1977) and the fugacity coefficient of Huizenga (1995) at 200 MPa in the liquid-carbonic inclusions (type-IIA and type-IIB fluid inclusions; Table 3).

Assuming that the following equilibrium reaction pertains to the ore fluids in the present study: (1) $CH_{4(g)} + 2O_{2(g)} \leftrightarrow CO_{2(g)} + 2H_2O_{(g)}$, then the oxygen fugacity of the fluids can be calculated as $\log fO_2 = 0.5*(\log fCO_2 + 2 \log fH_2O - \log fCH_4 - \log K_4)$ (for temperatures of 250–500°C and where log K = 81.1 at 250°C and 45.8 at 500°C: Ohmoto & Kerrick 1977). The calculated values of $\log fO_2$ (MPa) shown in Table 3 are from reaction (1), type-IIA (–1.99 to –3.11 MPa) and type-IIB (–3.01 to –3.74 MPa). The results give lower limits of fO_2 for the ore-bearing fluids in the Meiduk deposit. The ore-forming fluids are in a relatively oxidised state and high XCO_2 (average 0.16) during stage 1, which is supported by the absence of magnetite and minor pyrrhotite in the mineral assemblages. In oxidised states (e.g., stage 1) CO_2 and H_2O are dominant species, leaving ferrous iron as the sole reducing agent (Sun *et al.*, 2013). Therefore, ferrous-iron oxidation during magnetite crystallisation is critical for sulphate reduction and copper mineralisation (Sun *et al.*, 2013).

The general association of porphyry copper deposits with relatively oxidised magnetite-series (I-type) granitoids implies that the derived fluids will tend to be enriched in $\delta^{34}S$ values up to 4‰ higher than the source magma (Hassanzadeh, 1993: $\delta^{34}S$ = +6.1 to + 13.4‰; and

Table 3. Calculated bulk composition and oxygen fugacity for liquid-carbonic inclusions (IIA and IIB inclusion types) in ore-bearing quartz veins from Meiduk mine.

inclusion types	vein type (stage)	phase	XCO_2	XH_2O	XNaCl	log fO_2 (MPa)
IIA	A (1)	L_1+L_2+V	0.175	0.794	0.0309	–2.49
IIA	A (1)	L_1+L_2+V	0.12	0.871	0.008	–2.75
IIA	A (1)	L_1+L_2+V	0.146	0.839	0.014	–3.05
IIA	A (1)	L_1+L_2+V	0.12	0.859	0.02	–2.58
IIA	A (1)	L_1+L_2+V	0.206	0.779	0.014	–2.72
IIA	A (1)	L_1+L_2+V	0.146	0.844	0.009	–2.37
IIA	A (1)	L_1+L_2+V	0.175	0.813	0.011	–2.43
IIA	A (1)	L_1+L_2+V	0.073	0.895	0.031	–2.21
IIA	A (1)	L_1+L_2+V	0.146	0.831	0.022	–2.44
IIA	A (1)	L_1+L_2+V	0.75	0.81	0.014	–2.72
IIA	A (1)	L_1+L_2+V	0.12	0.865	0.014	–2.41
IIA	A (1)	L_1+L_2+V	0.207	0.784	0.008	–2.13
IIA	A (1)	L_1+L_2+V	0.12	0.848	0.031	–2.89
IIA	A (1)	L_1+L_2+V	0.175	0.798	0.026	–2.64
IIA	A (1)	L_1+L_2+V	0.146	0.827	0.026	–2.08
IIA	A (1)	L_1+L_2+V	0.12	0.862	0.017	–2.90
IIA	A (1)	L_1+L_2+V	0.073	0.914	0.012	–2.95
IIA	A (1)	L_1+L_2+V	0.12	0.871	0.008	–2.61
IIA	A (1)	L_1+L_2+V	0.034	0.955	0.011	–3.11
IIA	A (1)	L_1+L_2+V	0.073	0.908	0.017	–2.74
IIA	A (1)	L_1+L_2+V	0.241	0.731	0.027	–1.99
IIA	A (1)	L_1+L_2+V	0.175	0.798	0.026	–2.55
IIA	A (1)	L_1+L_2+V	0.175	0.796	0.029	–1.99
IIA	A (1)	L_1+L_2+V	0.206	0.766	0.027	–2.07
IIA	A (1)	L_1+L_2+V	0.12	0.85	0.029	–2.13
IIA	A (1)	L_1+L_2+V	0.073	0.906	0.02	–2.97
IIA	A (1)	L_1+L_2+V	0.175	0.806	0.018	–2.02
IIA	A (1)	L_1+L_2+V	0.12	0.868	0.011	–2.04
IIA	A (1)	L_1+L_2+V	0.073	0.914	0.011	–3.03
IIA	A (1)	L_1+L_2+V	0.175	0.804	0.02	–2.01
IIB	B (2)	L_1+L_2+V	0.12	0.855	0.025	–3.24
IIB	B (2)	L_1+L_2+V	0.073	0.919	0.006	–3.74
IIB	B (2)	L_1+L_2+V	0.073	0.904	0.022	–3.53
IIB	B (2)	L_1+L_2+V	0.074	0.904	0.021	–3.72
IIB	B (2)	L_1+L_2+V	0.034	0.932	0.033	–3.28
IIB	B (2)	L_1+L_2+V	0.073	0.915	0.011	–3.67
IIB	B (2)	L_1+L_2+V	0.073	0.905	0.021	–3.25
IIB	B (2)	L_1+L_2+V	0.034	0.94	0.026	–3.32
IIB	B (2)	L_1+L_2+V	0.073	0.9	0.026	–3.46
IIB	B (2)	L_1+L_2+V	0.073	0.903	0.022	–3.45
IIB	B (2)	L_1+L_2+V	0.12	0.857	0.022	–3.18
IIB	B (2)	L_1+L_2+V	0.0737	0.905	0.021	–3.50
IIB	B (2)	L_1+L_2+V	0.0737	0.904	0.022	–3.53
IIB	B (2)	L_1+L_2+V	0.0737	0.908	0.018	–3.53
IIB	B (2)	L_1+L_2+V	0.175	0.812	0.012	–3.01
IIB	B (2)	L_1+L_2+V	0.12	0.864	0.015	–3.68
IIB	B (2)	L_1+L_2+V	0.12	0.864	0.015	–3.57

Notes: XCO_2, XH_2O, XNaCl= mole fractions of CO_2, H_2O and NaCl estimated from microthermometric data and log fO_2= oxygen fugacity estimated from the reaction $CH_{4(g)} + 2O_{2(g)} <=> CO_{2(g)} + 2H_2O_{(g)}$ for H_2O-CO_2-bearing inclusions.

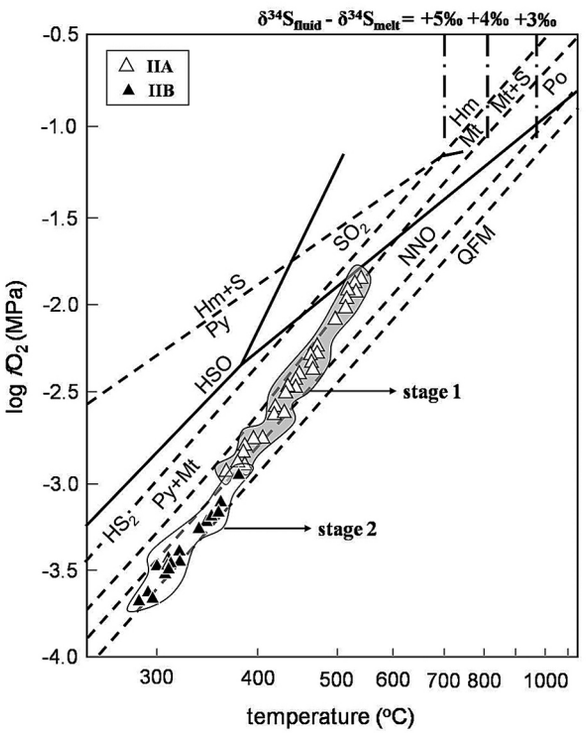

Fig. 7. Log fO_2-temperature plot showing oxygen fugacities of the mineralising fluid from the Meiduk deposit (stage 1: IIA inclusions; and stage 2: IIB) at 281–530 °C, estimated from the CO_2-CH_4 equilibrium. The QFM (quartz-fayalite-magnetite) and NNO (nickel/nickel-oxide) buffer curves below 300 °C were extrapolated from Nwe & Morteani (1993). The equilibrium constants are from Ohmoto & Kerrick (1977) and the fugacity coefficients of H_2O, CO_2, and CH_4 at 200 Mpa are from Huizenga (1995). Mineral-phase boundary lines are from McCuaig & Kerrich (1998). Abbreviations: Hm = hematite, Mt = magnetite, Po = pyrrhotite, Py = pyrite.

Taghipour, 2007: $\delta^{34}S$ = +11.5 to +19.4‰; Fig. 7).

As shown in Figure 7, the estimated log fO_2 from the type-A veins (stage 1) indicate that the initial fluids were derived from a highly oxidised magmatic system (values of log fO_2 > QFM), with oxygen fugacities (fO_2) between the nickel/nickel-oxide (NNO) and magnetite/hematite oxygen (MH) buffers. In contrast, log fO_2 values from the type-B veins (stage 2), fall along the QFM (quartz-fayalite-magnetite) buffer line, which is consistent with the observed ore mineral assemblages (Fig. 7). Therefore, the ore-forming fluid was in a relatively reduced state and low XCO_2 (average 0.08) during the main mineralisation (stage 2).

The mineralisation involved further reduction of S_3^- to S_2^{2-}, HS^-, etc, which also required oxidation of ferrous iron to magnetite, and lower pH values. This is probably responsible for triggering the potassic-sericitic alteration (stage 2) at lower pH values (Sun *et al.*, 2013):

$$2S_3^- + 20H_2O + 15Fe^{2+} = 6HS^- + 5Fe_3O_4 + 34H^+$$

Magnetite formed during this process usually coexists with sulphides (e.g., chalcopyrite-pyrite-bornite-pyrrhotite). Therefore, ferrous-iron oxidation during magnetite crystallisation is of critical importance for sulphate reduction and copper mineralisation. The optimal initial oxygen fugacity for porphyry copper deposits should be lower than the magnetite/hematite buffer; otherwise there will be no ferrous iron in the system. A low oxygen fugacity is favourable for copper porphyry mineralisation (Sun *et al.*, 2013).

7.2. Origin of the CO_2 and mineralisation processes

Studies of the Circum-Pacific porphyry copper deposits indicate that porphyry systems typically contain aqueous fluid inclusions with or without daughter minerals (Redmond *et al.*, 2004; Klemm *et al.*, 2007, 2008), and with no or minor fluid inclusions that are rich in pure CO_2 or CO_2-bearing(Cline & Bodnar, 1991; Bodnar, 1995; Ulrich *et al.*, 2001; Lu *et al.*, 2004). Abundant CO_2-rich fluid inclusions have, however, recently been reported from most porphyry systems formed in intracontinental tectonic settings (e.g., China and Tibet: Chen & Li, 2009; Chen & Wang, 2011; Yang *et al.*, 2013), particularly from a continental-collision setting such as the Meiduk deposit.

On the basis of the tectonic setting and geochemical characteristics, Chen & Li (2009) and Chen & Wang (2011) suggested that the ore-forming fluid of magmatic arcs (e.g., the Circum-Pacific region) were generated mainly from metamorphic dehydration of subducted oceanic slab. Such fluids could be somewhat enriched in NaCl brine, H_2O, Na and Cl, but depleted in CO_2 (or carbonate), K and F. In contrast,

porphyry copper systems formed in a collisional tectonic regime such as the Meiduk deposit in the KCMA originate from the partial melting of a thickened juvenile lower crust or lithospheric mantle, and they are poor in H_2O and NaCl, and they have high CO_2/H_2O, K/Na, F/Cl ratios in comparison to the subducting oceanic slab.

Shafiei *et al.* (2009) considered that the KCMA and their prospects (e.g., the Meiduk porphyry) were derived from partial melting of a thickened juvenile mafic lower crust. Therefore, the ore-forming fluid system at the Meiduk deposit was rich in CO_2 and evidently resulted in the development of abundant fluid inclusions of type-IIA, type-IIB and daughter minerals and CO_2-bearing fluid inclusions (Yang *et al.*, 2012, 2013).

Following the criteria proposed by Martin *et al.* (2005) and Castillo (2006, 2012), many geochemical features of the Meiduk porphyry in the KCMA, such as the moderate Mg number (average 43), the high Sr (>554 ppm), the low Y (<21 ppm), the low Yb (<1.4 ppm), and the high K (>2%) contents, the absence of an Eu anomaly, and the moderately high Sr/Y (>56) and La/Yb (>20) ratios are similar to adakitic rocks (Asadi, 2013). A close relationship between adakites and porphyry ore deposits (Cu, Mo, Au) was proposed by several authors (e.g., Mungall, 2002; Conly *et al.*, 2006; Richards & Kerrich, 2007). Fluid exsolved from this magma (stage 1) is characterised by CO_2-rich, high-temperature, low-salinity and Cu-rich properties. The fluid percolated through and reacted with the cooling porphyry rocks and their host (Razak volcanics), causing early potassic alteration (biotite and K-feldspar) and forming stockworks containing quartz and minor Cu sulphides (type-A veins). In stage 1, the early fluids were relatively oxidising (from –1.9 to –3.1 MPa) and S^{2-} poor, and therefore, unfavourable for sulphide deposition and copper mineralisation. Also, a high pressure (>100 MPa) prevented phase separation (boiling) during the early stage of mineralisation (Fig. 8).

Because of the consumption of alkali ions and the escape of CO_2 ($2H^+ + CO_3^{2-} \rightarrow H_2O + CO_2\uparrow$) in stage 1, the fluid became more acidic, reducing and rich in S^{2-}. According to Lowenstern (2001) and Yang *et al.* (2013), the fO_2 of the ore-fluid decreased (from –3.0 to –3.7 MPa) due to the precipitation of abundant sulphide minerals and magnetite and escape of CO_2, resulting in an increase in S^{2-} activity during stage 2. Accompanied by further cooling of the Meiduk porphyry, boiling and hydraulic fracturing, the meteoric water percolated into and mixed with the magmatic hydrothermal system (Fig. 8). The fluid boiling characterised by CO_2 escape and mixing with meteoric water are two key factors resulting in the deposition of sulphides or ore-metals (Robb, 2005; Li *et al.*, 2012; Yang *et al.*, 2013; Asadi *et al.*, 2013).

Therefore, the homogenisation temperatures became lower in stage 2than in stage 1

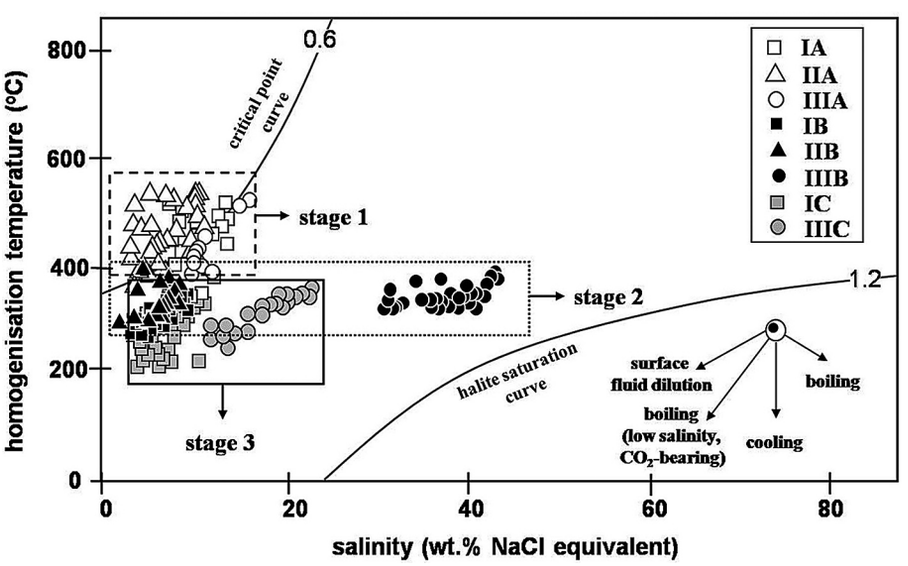

Fig. 8. Homogenisation temperatures for about 210 fluid inclusions against their salinity in quartz from three quartz veins at the Meiduk deposit. The critical-point and halite-saturation curves show the densities ($g \cdot cm^{-3}$) of the fluid inclusions (after Wilkinson, 2001).

and salinities of fluid inclusions displayed a trend of increasing salinity (Fig. 8). The fluids became less carbonic, which is indicated by the decrease of the volume proportions of the CO_2 phase in type-IIB inclusions. These changes of ore-forming fluid facilitated the deposition of sulphides, together with potassic-sericitic alteration and quartz-sulphide stockworks (type-B veins). Laser Raman spectroscopy also confirms that the gas content of fluid inclusions (e.g., CO_2 and CH_4) decreased with decreasing depth (Fig. 6), possibly consistent with gas loss during boiling in the Meiduk porphyry system.

In stage 3, the fluids got more dilute and CO_2-poor, and therefore none of the type-II three-phase liquid-carbonic inclusions (LH_2O+LCO_2+V) were present. This stage represented the waning ore-forming process during sericitic hydrothermal alteration with quartz-sulphide stockworks (type-C veins) that resulted from CO_2-poor, low-temperature and dilute hydrothermal fluids derived from meteoric-hydrothermal waters (Fig. 8).

8. Conclusions

The Meiduk porphyry copper system, which is located in the collisional Kerman Cenozoic magmatic arc (KCMA), is associated with intrusive rocks of Miocene age that intruded the Eocene Razak volcanic complex. The mineralisation process included three stages, characterised by early potassic alteration: quartz + K-feldspar + biotite + pyrite ± chalcopyrite ± pyrrhotite ± magnetite (stage 1 and type-A veins), potassic-sericitic alteration: quartz + chalcopyrite + pyrite + bornite + pyrrhotite + K-feldspar + biotite + magnetite (stage 2 and B-type veins), and sericitic alteration: quartz + pyrite + chalcopyrite + sericite (stage 3 and type-C veins). Most ores were formed during stages 2 and 3.

Three main fluid inclusions types are distinguished in the hydrothermal quartz veins of the Meiduk deposit: liquid + vapour ± solid (type I), $LH_2O + LCO_2 + V$ (type II) and multi-phase solid inclusions (type III). Types I and III are characteristic of all porphyry copper systems, but type II is distinctive of the porphyry copper deposits formed in a continental collision regime (e.g., the Meiduk deposit).

Microthermometrical results indicate that the homogenisation temperatures of the fluid inclusions gradually decreased from 530–340°C (stage 1), through 385–270°C (stage 2), to 350–214°C (stage 3). The estimated trapping pressures were <120 MPa in stage 1 and <80 MPa in stage 2, suggesting a mineralisation depth of approx. 3 km.

The CO_2-bearing fluid of the Meiduk system is a distinctive feature related to a continental-collision setting. Based on the criteria of Lowenstern (2001), Robb (2005), Yang *et al.*, (2012, 2013) and Sun *et al.* (2013), degassing of CO_2 from the CO_2-rich magma and the high ratio of CO_2/H_2O in fluids resulted in a low NaCl activity in the initial ore-forming fluids, causing paucity of halite-bearing inclusions, distinctive of hydrothermal quartz veins during stage 1. The CO_2/H_2O ratio typically decreased during progressive decompression or crystallisation-induced degassing. Therefore, CO_2-escape was an important factor in (1) increasing the activity of NaCl, S^{2-} and the boiling process in the fluids, (2) reducing the initial oxidation of the fluids, and (3) precipitation of sulphide minerals in the Meiduk quartz veins during stages 2 and 3.

Acknowledgements

This contribution represents part of the Ph.D. thesis of S.A. at Shiraz University, Iran. Logistic and financial support was provided by the Research and Development Centre of National Iranian Cu Industries (NICICo.) at the Sarcheshmeh mine. We are grateful to M.R Ramezani (Meiduk mine) for providing core samples of the Meiduk Cu deposit. We would like to extend our thanks to Professor David Lentz (New Brunswick University) which pre-reviewed the manuscript.

References

Ahmadian, J., Haschke, M., McDonald, I., Regelous, M., Ghorbani, M., Emami, M. & Murata, M., 2009. High magmatic flux during Alpine-Himalayan collision: Constraints from the Kal-e-Kafi complex, central Iran. *Geological Society of America Bulletin* 121, 857–868.

Alavi, M., 2007. Structure of the the Zagros fold-thrust belt in Iran. *American Journal of Science* 307, 1064–1095.

Asadi, S., 2013. Selective geochemistry of barren and productive porphyry copper deposits in Urumiyeh-Dokhtar volcano-magmatic belt. *National Iranian Copper Industries Company Internal Report (258/M/90/D)* 2, 22–45.

Asadi, S., Moore, F. & Fattahi, N., 2013. Fluid inclusion and stable isotope constraints on the genesis of the Jian copper deposit, Sanandaj–Sirjan metamorphic zone, Iran. *Geofluids* 13, 66–81.

Bakker, R.J., 2003. Package FLUIDS 1. Computer programs for analysis of fluid inclusion data and for modelling bulk fluid properties. *Chemical Geology* 194, 3–23.

Bodnar, R.J., 1993. Revised equation and table for determining the freezing point depression of H_2O-NaCl solutions. *Geochimica et Cosmochimica Acta* 57, 683–684.

Bodnar, R.J., 1995. Fluid inclusion evidence for a magmatic source for metals in porphyry copper deposits. *Mineralogical Association of Canada Short Course Series* 23, 139–152.

Boomeri, M., Nakashima, K. & Lentz, D.R., 2009. The Miduk porphyry Cu deposit, Kerman, Iran: a geochemical analysis of the potassic zone including halogen element systematics related to Cu mineralization processes. *Journal of Geochemical Exploration* 103, 17–29.

Bowers, T.S. & Helgeson, H.C., 1983. Calculation of the thermodynamic and geochemical consequences of nonideal mixing in the system H_2O-CO_2-NaCl on phase relations in geological systems: equation of state for H_2O-CO_2-NaCl fluids at high pressures and temperatures. *Geochimica et Cosmochimica Acta* 47, 1247–1275.

Brown, P.E., 1989. Flincor: a microcomputer program for the reduction and investigation of fluid inclusion data. *American Mineralogist* 74, 1390–1393.

Brown, P.E. & Hagemann, S.G., 1994. MacFlinCor: A computer program for fluid inclusion data reduction and manipulation. [In:] B. De Vivo & M.L. Frezzotti (Eds): *Fluid inclusions in minerals: methods and applications.* International Mineralogical Association 16th Short Course of the Working Group, Portignano–Siena, Italy, 231–250.

Burke, E.A.J., 2001. Raman microspectrometry of fluid inclusions. *Lithos* 55, 139–158.

Castillo, P.R., 2006. An overview of adakite petrogenesis. *Chinese Science Bulletin* 51, 257–268.

Castillo, P.R., 2012. Adakite petrogenesis. *Lithos* 135, 304–316.

Chen, Y.J. & Fu, S.G., 1992. *Gold mineralization in West Henan, China.* China Seismological Press, Beijing, 234 pp.

Chen, Y.J. & Wang, Y., 2011. Fluid inclusion study of the Tangjiaping Mo deposit, Dabie Shan, Henan Province: implications for the nature of porphyry systems of postcollisional tectonic settings. *International Geology Review* 53, 635–655.

Chen, Y.J., Ni, P., Fan, H.R., Pirajno, F., Lai, Y., Su, W.C. & Zhang, H., 2007. Diagnostic fluid inclusions of different types hydrothermal gold deposits. *Acta Petrologica Sinica* 23, 2085–2108.

Chen,Y.J. & Li, N., 2009. Diagnostic fluid inclusion and wallrock alteration of intrusionrelated hypothermal ore-systems (porphyry, skarn, breccia pipe, vein and IOCG) formed in intracontinental settings: origin and difference from those in volcanic arc. *Acta Petrologica Sinica* 25, 2477–2508.

Cline, J.S. & Bodnar, R.J., 1991. Can economic porphyry copper mineralization be generated by a typical calc-alkaline melt? *Journal of Geophysical Research* 96, 8113–8126.

Collins, P.L.F., 1979. Gas hydrates in CO_2-bearing fluid inclusions and the use of freezing data for estimation of salinity. *Economic Geology* 74, 1435–1444.

Conly, A.G., Beaudoin, G. & Scott, S.D., 2006. Isotopic constraints on fluid evolution and precipitation mechanisms for the Boléo Cu–Co–Zn district, Mexico. *Mineralium Deposita* 41, 27–151.

Dehghani, G.A. & Makris, T., 1983. The gravity field and crustal structure of Iran. *Geological Survey of Iran Report* 51, 51–68.

Dercourt, J., Zonenshain, L., Ricou, L.E., Kazmin, G., LePichon, X., Knipper, A.L., Grandjacquet, C., Sbortshikov, I.M., Geyssant, J., Lepvrier, C., Pechersky, D.H., Boulin, J., Sibuet, J.C., Savostin, L.A., Sorokhtin, O., Westphal, M., Bazhenov, M.L., Lauer, J.P. & Biju-Duval, B., 1986. Geological evolution of the Tethys belt from the Atlantic to Pamirs since the Lias. *Tectonophysics* 123, 241–315.

Dewey, J.F., Pitman, W.C., Ryan, W.B. & Bonnin, J., 1973. Plate tectonics and the evolution of the Alpine system. *Geological Society of America Bulletin* 84, 3137–3180.

Dimitrijevic, M.D., 1973. Geology of the Kerman region. *Geological Survey of Iran Report* 52, 245–334.

Dreher, A.M., Xavier, R.P., Taylor, B.E. & Martini, S., 2007. New geologic, fluid inclusion and stable isotope studies on the controversial Igarapé Bahia Cu–Au deposit, Carajás Province, Brazil. *Mineralium Deposita* 43, 161–184.

Dubessy, J., Buschaert, S., Lamb, W., Pironon, J. & Thiery, R., 2001. Methane-bearing aqueous fluid inclusions: raman analysis, thermodynamic modeling and application to petroleum basins. *Chemical Geology* 173, 193–205.

Fan, H.R., Hu, F.F., Wilde, S.A., Yang, K.F. & Jin, C.W., 2011. The Qiyugou gold-bearing breccia pipes, Xiong'ershan region, central China: fluid inclusion and stable isotope evidence for an origin from magmatic fluids. *International Geology Review* 53, 25–45.

Guild, P.W., 1972. Metallogeny and the new global tectonics. *International Geological Congress Proceedings* 4, 17–24.

Hall, D.L., Sterner, S.M. & Bodnar, R.J., 1988. Freezing point depression of NaCl–KCl–H_2O solutions. *Economic Geology* 83, 197–202.

Haschke, M., Ahmadian, J., Murata, M. & McDonald, I., 2010. Copper mineralization prevented by arc-root delamination during Alpine-Himalayan collision in central Iran. *Economic Geology* 105, 855–865.

Hassanzadeh, J., 1993. Metallogenic and tectono-magmatic events in the SE sector of the Cenozoic active continental margin of Iran (Shahr e Babak area, Ker-

man province). Unpublished Ph.D. thesis. University of California, 204 pp.

Hezarkhani, A., 2008. Hydrothermal evolution of the Miduk porphyry copper system, Kerman, Iran: a fluid inclusion investigation. *International Geology Review* 50, 665–684.

Hou, Z.Q. & Cook, N.J., 2009. Metallogenesis of the Tibetan collisional orogen: a review and introduction to the special issue. *Ore Geology Reviews* 36, 2–24.

Hou, Z.Q., Gao, Y.F., Qu, X.M., Rui, Z.Y. & Mo, X.X., 2004. Origin of adakitic intrusives generated during mid-Miocene east–west extension in southern Tibet. *Earth and Planetary Science Letters* 220, 139–155.

Hou, Z.Q., Zhang, H., Pan, X. & Yang, Z., 2011. Porphyry Cu (–Mo–Au) deposits related to melting of thickened mafic lower crust: examples from the eastern Tethyan metallogenic domain. *Ore Geology Reviews* 39, 21–45.

Huizenga, J.M., 1995. *Fluid evolution in shear zones from the Late Archean Harare-Shamva-Bindura greenstone belt (NE Zimbabwe): thermodynamic calculations of the C-O-H system applied to fluid inclusions.* Netherlands Research School of Sedimentary Geology Press, Amsterdam, 146 pp.

Hurai, H., Kihle, J., Kotulova, J., Marko, F.S. & Wierczewska, A., 2002. Origin of methane in quartz crystals from the Tertiary accretionary wedge and fore-arc basin of the Western Carpathians. *Applied Geochemistry* 17, 1259–1271.

IGME-INOMRM (Institute for Geological & Mining Exploration & Institution of Nuclear and Other Mineral Raw Materials), 1973. Exploration for ore deposits in Kerman Region. *Iran Geological Survey Report No. Yu/53*; *Iran Geological Survey (Beograd, Yugoslavia)*, 247 pp.

Karsli, O., Dokuz, A., Uysal, I., Aydin, F., Kandemir, R. & Wijbrans, R.J., 2010. Generation of the Early Cenozoic adakitic volcanism by partial melting of mafic lower crust, eastern Turkey: implications for crustal thickening to delamination. *Lithos* 114, 109–120.

Kirkham, R.V. & Dunne, K.P., 2000. World distribution of porphyry, porphyry-associated skarn, and bulk-tonnage epithermal deposits and occurrences. *Geological Survey of Canada Report* 3792, 1–26.

Klemm, L.M., Pettke, T. & Heinrich, C.A., 2008. Fluid and source magma evolution of the Questa porphyry Mo deposit, New Mexico, USA. *Mineralium Deposita* 43, 533–552.

Klemm, L.M., Pettke, T., Heinrich, C.A. & Campos, E., 2007. Hydrothermal evolution of the El Teniente deposit, Chile: porphyry Cu–Mo ore deposition from low-salinity magmatic fluids. *Economic Geology* 102, 1021–1045.

Landtwing, M.R., Furrer, C., Redmond, P.B., Pettke, T., Guillong, M. & Heinrich, C.A., 2010. The Bingham Canyon porphyry Cu–Mo–Au deposit. III. Zoned copper–gold ore deposition by magmatic vapor expansion. *Economic Geology* 105, 91–118.

Landtwing, M.R., Pettke, T., Halter, W.E., Heinrich, C.A., Redmond, P.B., Einaudi, M.T. & Kunze, K., 2005. Copper deposition during quartz dissolution by cooling magmatic–hydrothermal fluids: the Bingham porphyry. *Earth and Planetary Science Letters* 235, 229–243.

Li, N., Carranza, E.J.M., Ni, Z.Y. & Guo, D.S., 2012. The CO_2-rich magmatic-hydrothermal fluid of the Qiyugou breccia pipe, Henan Province, China: implication for breccia genesis and gold mineralization. *Geochemistry: Exploration, Environment, Analysis* 12, 147–160.

Liang, H.Y., Sun, W.D., Su, W.C. & Zartman, R.E., 2009. Porphyry copper–gold mineralization at Yulong, China, promoted by decreasing redox potential during magnetite alteration. *Economic Geology* 104, 587–596.

Lowenstern, J.B., 2001. Carbon dioxide in magmas and implications for hydrothermal systems. *Mineralium Deposita* 36, 490–502.

Lu, H.Z., Fan, H.R., Ni, P., Ou, G.X., Shen, K. & Zhang, W.H., 2004. *Fluid inclusions*. Science Press, Beijing, 78 pp.

Martin, H., Smithies, R.H., Rapp, R., Moyen, J.F. & Champion, D., 2005. An overview of adakite, tonalite-trondhjemite-granodiorite (TTG), and sanukitoid: relationships and some implications for crustal evolution. *Lithos* 79, 1–24.

McClay, K.R., Whitehouse, P.S., Dooley, T. & Richards, M., 2004. 3D evolution of fold and thrust belts formed by oblique convergence. *Marine Geology* 21, 857–877.

McClusky, S., Balassanian, S., Barka, A., Demir, C., Ergintav, S., Georgiev, I., Gurkan, O., Hamburger, M., Hurst, K., Kahle, H., Kastens, K. & Kekelidze, G., 2000. Global positioning system constrains on plate kinematics and dynamics in the eastern Mediterranean and Caucasus. *Journal of Geophysical Research* 105, 5695–5719.

McCuaig, T.C. & Kerrich, R., 1998. P-T-t-deformation-fluid characteristics of lode gold deposits: evidence from alteration systematics. *Ore Geology Reviews* 12, 381–453.

McInnes, B.I.A., Evans, N.J., Fu, F.Q., Garwin, S., Belousova, E., Griffin, W.L., Bertens, A., Sukarna, D., Permanadewi, S., Andrew, R.L. & Deckart, D., 2005. Thermal history analysis of selected Chilean, Indonesian, and Iranian porphyry Cu–Mo–Au deposits. [In:] T.M. Porter (Ed.): *Super porphyry copper and gold deposits: a global perspective*. PGC Publishing, Adelaide, 1–16.

Mohajjel, M., Fergusson, C.L. & Sahandi, M.R., 2003. Cretaceous–Tertiary convergence and continental collision, Sanandaj–Sirjan zone, western Iran. *Journal of Asian Earth Sciences* 21, 397–412.

Moore, F., 1992. Fluid inclusion studies and mineralization at Meiduk porphyry copper deposit, Kerman. *National Iranian Copper Industries Company Report* 8, 1–26.

Mungall, J.E., 2002. Roasting the mantle: slab melting and the genesis of major Au and Au-rich Cu deposits. *Geology* 30, 915–918.

Nwe, Y.Y. & Morteani, G., 1993. Fluid evolution in the H_2O-CH_4-CO_2-NaCl system during emerald mineralization at Gravelotte, Murchison greenstone belt, Northeast Transvaal, South Africa. *Geochimica et Cosmochimica Acta* 57, 89–103.

Ohmoto, H. & Kerrick, D., 1977. Devolatilization equilibria in graphitic systems. *American Journal of Science* 277, 1013–1044.

Pirajno, F., 2009. *Hydrothermal processes and mineral systems*. Springer, Heidelberg, 1250 pp.

Razique, A.L., Grasso, G. & Livesey, T., 2007. Porphyry copper–gold deposits at Reko Diq complex, Chagai Hills Pakistan. *Proceedings of Ninth Biennial SGA Meeting (Dublin),* 1–7.

Redmond, P.B., Einaudi, M.T., Inan, E.E., Landtwing, M.R. & Heinrich, C.A., 2004. Copper deposition by fluid cooling in intrusion-centered systems: new insights from the Bingham porphyry ore deposit, Utah. *Geology* 32, 217–220.

Richards, J.P., Spell, T., Rameh, E., Razique, A. & Fletcher, T., 2012. High Sr/Y magmas reflect arc maturity, high magmatic water content, and porphyry Cu ± Mo ± Au potential: examples from the Tethyan arcs of central and eastern Iran and western Pakistan. *Economic Geology* 107, 295–332.

Richards, J.R. & Kerrich, R., 2007. Adakite-like rocks: their diverse origins and questionable role in metallogenesis. *Economic Geology* 102, 537–576.

Robb, L., 2005. *Introduction to ore-forming processes*. Blackwell Publishing, Oxford, 386 pp.

Roedder, E., 1984. Fluid inclusions, reviews in mineralogy. *Mineralogical Society of America* 12, 325–340.

Rusk, B. & Reed, M., 2002. Scanning electron microscope-cathodoluminescence analysis of quartz reveals complex growth histories in veins from the Butte porphyry copper deposit, Montana. *Geology* 30, 727–730.

Rusk, B., Reed, M. & Dilles, J., 2008. Fluid inclusion evidence for magmatic-hydrothermal fluid evolution in the porphyry copper-molybdenum deposit at Butte, Montana. *Economic Geology* 103, 307–334.

Saric, V. & Mijalkovic, N., 1973. Metallogenic map of Kerman region, 1:500000 scale. Exploration for ore deposits in Kerman region. *Geological Survey of Iran Report* 53, 244–247.

Shafiei, B., Haschke, M. & Shahabpour, J., 2009. Recycling of orogenic arc crust triggers porphyry Cu mineralization in Kerman Cenozoic arc rocks, southeastern Iran. *Mineralium Deposita* 44, 265–283.

Shafiei, B., 2008. Metallogenic model for Kerman porphyry copper belt and its implications for exploration. Unpublished Ph.D. Thesis. University of Kerman (Shaheed Bahonar), Iran, 257 pp.

Shafiei, B., 2010. Lead isotope signatures of the igneous rocks and porphyry copper deposits from the Kerman Cenozoic magmatic arc (SE Iran), and their magmatic-metallogenetic implications. *Ore Geology Reviews* 38, 27–36.

Shahabpour, J., 2005. Tectonic evolution of the orogenic belt in the region located between Kerman and Neyriz. *Journal of Asian Earth Sciences* 24, 405–417.

Shen, P., Shen, Y., Wang, J., Zhu, H., Wang, L. & Meng, L., 2010. Methane-rich fluid evolution of the Baogutu porphyry Cu–Mo–Au deposit, Xinjiang, NW China. *Chemical Geology* 275, 78–98.

Shepherd, T.J., Rankin, A.H. & Alderton, D.H.M., 1985. *A practical guide to fluid inclusion studies*. Blackie Press, London, 239 pp.

Sun, W.D., Arculus, R.J., Kamenetsky, V.S. & Binns, R.A., 2004. Release of gold-bearing fluids in convergent margin magmas prompted by magnetite crystallization. *Nature* 431, 975–978.

Sun, W.D., Liang, H.Y., Ling, M.X., Zhan, M.Z., Ding, X., Zhang, H., Yang, X.Y., Li, Y.L., Ireland, T.R., Wei, Q.R. & Fan, W.M., 2013. The link between reduced porphyry copper deposits and oxidized magmas. *Geochimica et Cosmochimica Acta* 103, 263–275.

Taghipour, N., 2007. The application of fluid inclusions and isotope geochemistry as guides for exploration, alteration and mineralization at the Meiduk porphyry copper deposit, Shahr-Babak, Kerman. Unpublished Ph.D. Thesis. Shaheed Bahonar University (Kerman), Iran, 321 pp.

Taghipour, N., Aftabi, A. & Mathur, R., 2008. Geology and Re-Os geochronology of mineralization of the Miduk porphyry copper deposit, Iran. *Resource Geology* 2, 143–160.

Topuz, G., Okay, A.I., Altherr, R., Schwar, W.H., Siebel, W., Zack, T., Muharrem, S. & Cuneyt, S., 2011. Post-collisional adakite-like magmatism in the Ağvanis massif and implications for the evolution of the Eocene magmatismin the Eastern Pontides (NE Turkey). *Lithos* 125, 131–150.

Ulrich, T., Guenther, D. & Heinrich, C.A., 2001. The evolution of a porphyry Cu–Au deposit, based on LA-ICP-MS analysis of fluid inclusions: Bajo de la Alumbrera, Argentina. *Economic Geology* 96, 1743–1774.

Ulrich, T., Gunther, D. & Heinrich, C.A., 2002. Evolution of a porphyry Cu–Au deposit, based on LA-ICP-MS analysis of fluid inclusions: Bajo de la Alumbrera, Argentina. *Economic Geology* 97, 1863–1920.

Volkov, A.V., Savva, N.E., Sidorov, A.A., Prokofev, V.Y., Goryachev, N.A., Voznesensky, S.D., Al'Shevsky, A.V. & Chernova, A.D., 2011. Shkol'noe gold deposit, the Russian Northeast. *Geology of Ore Deposits* 53, 1–26.

Wang, L.L., Mo, X.X., Li, B., Dong, G.C. & Zhao, Z.D., 2006. Geochronology and geochemistry of the ore-bearing porphyry in Qulong Cu (Mo) ore deposit, Tibet. *Acta Petrologica Sinica* 22, 1001–1008.

Wilkinson, J.J., 2001. Fluid inclusions in hydrothermal ore deposit. *Lithos* 55, 229–272.

Yang, Y., Zhang, J., Yang, Y.F. & Shi, Y.X., 2009. Fluid inclusions geochemistry and ore genesis of Shangfanggou Mo–Fe deposit in Luanchuan County, Henan Province. *Acta Petrologica Sinica* 25, 2563–2574.

Yang, Y.F., Chen, Y.J., Li, N., Mi, M., Xu, Y.L., Li, F.L. & Wanc, S.Q., 2013. Fluid inclusion and isotope geochemistry of the Qian'echong giant porphyry Mo deposit, Dabie Shan, China: a case of NaCl-poor, CO_2-rich fluid systems. *Journal of Geochemical Exploration* 124, 1–13.

Yang, Y.F., Li, N. & Chen, Y.J., 2012. Fluid inclusion study of the Nannihu giant porphyry Mo–W deposit, Henan Province, China: implications for the nature of por-

phyry ore-fluid systems formed in a continental collision setting. *Ore Geology Reviews* 46, 83–94.

Zarasvandi, A., Liaghat, S. & Zentilli, M., 2005. Geology of the Darreh-Zerreshk and Ali-Abad porphyry copper deposit, central Iran. *International Geology Review* 47, 620–646.

Zarasvandi, A., Liaghat, S. Zentilli, M. & Reynolds, P.H., 2007. $^{40}Ar/^{39}Ar$ geochronology of alteration and petrogenesis of porphyry copper-related granitoids in the Darreh-Zerreshk and Ali-Abad area, central Iran. *Exploration and Mining Geology* 16, 11–24.

Zhang, Y. & Frantz, J.D., 1987. Determination of the homogenization temperatures and densities of supercritical fluids in the system NaCl-KCl-$CaCl_2$-H_2O using synthetic fluid inclusion. *Chemical Geology* 64, 335–350.

Zhong, J., Chen, Y.J., Chen, J., Li, N., Li, J., Qi, J.P. & Mao-Chang, D.A.I., 2011. Fluid inclusion study of Luoboling porphyry Cu–Mo deposit in Zijinshan ore field, Fujian Province. *Acta Petrologica Sinica* 27, 1410–1424.

Manuscript submitted 9 June 2013
Revision accepted 12 November 2013